

Evidence for magnetic dimers and skyrmion lattice formation in  $\text{Eu}_2\text{Pd}_2\text{Sn}$ J. G. Sereni<sup>1,\*</sup>, I. Čurlík<sup>2</sup>, M. Reiffers<sup>3,4</sup> and M. Giovannini<sup>5</sup><sup>1</sup>*Low Temperature Division, CAB-CNEA, CONICET, IB-UNCuyo, 8400 Bariloche, Argentina*<sup>2</sup>*Faculty of Humanities, University of Prešov, 17. novembra 1, SK - 080 78 Prešov, Slovakia*<sup>3</sup>*Faculty of Sciences, University of Prešov, 17. novembra 1, SK - 080 78 Prešov, Slovakia*<sup>4</sup>*Institute of Experimental Physics, Slovak Academy of Science, Watsonova 47, Košice, Slovakia*<sup>5</sup>*Department of Chemistry, University of Genova, Via Dodecaneso 31, Genova, Italy*

(Received 11 March 2023; revised 11 June 2023; accepted 12 July 2023; published 24 July 2023)

The magnetic, thermal, and transport properties of the noncentrosymmetric compound  $\text{Eu}_2\text{Pd}_2\text{Sn}$  are reexamined with the inclusion of detailed measurements. In its paramagnetic phase, the outstanding feature of this compound is the formation of  $\text{Eu}^{2+}$  dimers, which allows us to understand the deviation of the magnetic susceptibility  $\chi(T)$  from the Curie-Weiss law below about 70 K, the field-dependent magnetization  $M(B)$  below  $\approx 80$  K, and the reduced entropy at the ordering temperature  $S(T_N) = 0.64R \ln(8)$ . A significant change in the exchange interactions occurs between  $T \approx 70$  K (where  $\theta_p = 18$  K) and  $T_N = 13.3$  K (to  $\theta_p = -4.5$  K). The strong electronic overlap, arising from the reduced Eu-Eu spacing (compared with that in pure  $\text{Eu}^{2+}$ ) is expected to favor dimer quasiparticles formation, leading to a significant change in the magnetic structure. From the analysis of the derivatives of the magnetic parameters,  $\partial\chi/\partial T$  and  $\partial M/\partial B$ , as well as the field dependence of the specific heat and magnetoresistance, a comprehensive magnetic phase diagram is obtained. Two critical points are recognized and a tentative description of the magnetic structures is proposed. The possible formation of a skyrmion lattice, arising from the presence of magnetically frustrated pockets in the phase diagram, is suggested by theoretical studies on hexagonal structures that exhibit similar interaction patterns.

DOI: [10.1103/PhysRevB.108.014427](https://doi.org/10.1103/PhysRevB.108.014427)

## I. INTRODUCTION

Most ternary rare earth (RE) compounds exhibit ground states (GS) with low degeneracy owing to the effect of crystalline electric field (CEF). Depending on the integer or half-integer character of their total angular momentum  $J$  and local symmetry, their GS do not exceed a fourfold degeneracy (as in cubic structures). Consequently, their effective magnetic moments  $\mu_{\text{eff}}$  at low temperatures are much lower than at high temperatures because the magnetic order usually occurs at lower temperature than the level splitting induced by the CEF.

The well-known exception to this effect is the pure spin  $\text{Gd}^{3+}$  with a  $[\text{Xe}][6s^2 5d^1 4f^7]$  electron configuration, since with its  $J = S = 7/2$  and its orbital momentum  $L = 0$ , it is not affected by the symmetry reduction caused by the CEF. A similar case is  $\text{Eu}^{2+}$  in its excited electronic configuration  $[\text{Xe}][6s^2 4f^7]$ , which is currently considered equivalent to the  $\text{Gd}^{3+}$  for magnetic purposes.

However, the  $\text{Eu}^{2+}$  configuration is not identical to  $\text{Gd}^{3+}$  although it has the same number of  $4f$  electrons. This difference is reflected in some physicochemical properties such as their respective atomic radii: 2.04 Å for  $\text{Eu}^{2+}$  and 1.80 Å for  $\text{Gd}^{3+}$ , as well as their temperature and heat of melting [1]. As a consequence,  $\text{Eu}^{2+}$  may form a number of compounds normally allowed for large divalent alkaline earths (e.g.,  $\text{Ca}^{2+}$ ), but not for smaller  $\text{Gd}^{3+}$  atoms. Nevertheless, to our

knowledge there are no studies comparing the actual  $\text{Eu}(Z = 63)$   $[6s^2 4f^7]$  electronic “form factor” with that of  $\text{Gd}(Z = 64)$ .

Moreover, the absence of CEF effect allows both RE to exhibit the largest  $\mu_{\text{eff}}$  values among magnetic elements, making them good candidates for adiabatic demagnetization refrigeration processes [2]. This is the reason why there is a growing interest in the search of new  $\text{Eu}^{2+}$  ternary compounds [3–8]. In this paper we revisit the already-characterized  $\text{Eu}_2\text{Pd}_2\text{Sn}$  [9] in order to better understand its unusual magnetic behavior and to construct a tentative magnetic phase diagram. To this end, measurements were performed including detailed field-dependent magnetic susceptibility, magnetization, and low-temperature magnetoresistance.

One of the remarkable features of the crystal structure of  $\text{Eu}_2\text{Pd}_2\text{Sn}$  ( $\text{Ca}_2\text{Pd}_2\text{Sn}$  type [10]) is the noncentrosymmetric character of its orthorhombic structure, in which magnetic Eu nearest neighbors (Eu-NN at 3.734 Å [9]) form zig-zag chains, represented by brown lines connecting Eu atoms in Fig. 1(a). These chains lie along the “ac” plane, with Eu atoms alternately shifted up and down with respect to this plane, see Fig. 1(b). There, one can see how the Eu chains are stacked along the “b” direction, with two consecutive chains in the “b” direction belonging to an AB bilayer while the following pair belongs to an A'B' bilayer. The distinction between AB and A'B' bilayers arises from the fact that each bilayer encloses a linear Pd chain [10] pointing in to two alternating directions, as shown schematically in Fig. 1(c), where Eu and Sn atoms arranged in entangled chains represented by parallel cylinders. Each cylinder, whose axes are defined by linear Pd chains,

\*jsereni@yahoo.com

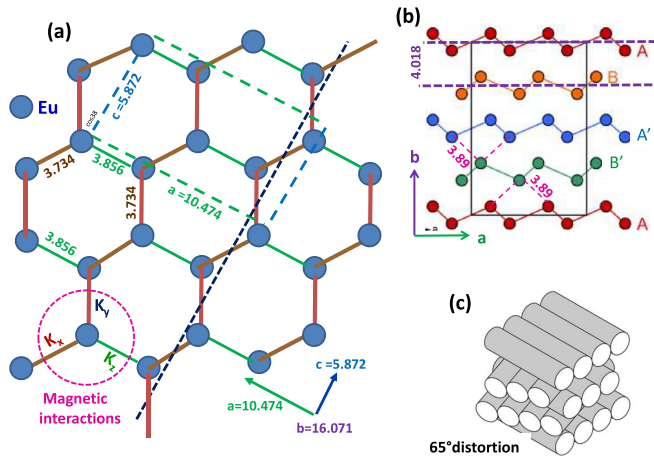


FIG. 1. (a) View of the Eu atoms network projected on the “ac” plane [10], including Eu-NN (brown segments) and Eu-NNN (green segments) distances: 3.734 Å and 3.856 Å respectively [9]. The blue-dashed long line connects the crossing points between Eu-NN lines with the “ac” plane. The green-dashed rectangle outlines the unit cell, and the magenta-dashed circle contains the neighboring magnetic interactions labeled as  $K_{x,y,z}$  according to Kitaev representation [11]. (b) Zig-zag Eu chains staked along the “b” direction and projected on the “ab” plane (dashed-brown lines). (c) Cylinder-like structural fragments representing Eu chains wrapping respective linear Pd chains (after Fig. 1 I-b of Ref. [9]) and forming a 65° dihedral between layers.

contains upper and lower zig-zag Eu chains that form the bilayers shown in Fig. 1(b) (labeled as AB or A'B'), while successive cylinders form a 65.2° dihedral [9] as shown in Fig. 1(c).

In Fig. 1(a), one can see that all neighboring chains lying in the same “ac” plane form a network of puckered-elongated hexagons. The elongated sides (green segments in the figure) correspond to the next-nearest-Eu neighbors (NNN at 3.856 Å [9]). Those puckered networks are arranged in a ABA'B' layers sequence as previously shown [10]. Notice that the mean distance between layers ( $L$ ) is  $LL = 4.018\text{Å}$ , see Fig. 1(b), but due to the puckered topology of the hexagonal network there are two Eu-third neighbors at  $Eu_{LL} = 3.89\text{Å}$ , both alternatively belonging to the upper and lower layer. In other words, if  $Eu_i$  atoms of chain B' in “even” positions ( $i = 0, 2, 4, \dots$ ) have both  $Eu_{LL}$  atoms on the upper (A') layer, the “odd” atoms ( $i = 1, 3, 5, \dots$ ) have them on the lower (A) layer that belongs to the following bilayer.

There is a further structural peculiarity in this compound. As mentioned before the Eu-NN spacing in  $\text{Eu}_2\text{Pd}_2\text{Sn}$  is 3.734 Å while the corresponding distance in pure  $\text{Eu}^{2+}$  metal is 4.08 Å [12]. The intensity of this electronic overlap can be evaluated by comparing this difference:  $(4.08 - 3.734)/4.08 \approx 8.5\%$ , with the one between  $\text{Eu}^{2+}$  and  $\text{Eu}^{3+}$  metals:  $\approx 11\%$ . Notably, despite such electronic overlap Eu atoms in  $\text{Eu}_2\text{Pd}_2\text{Sn}$  keep their expanded  $\text{Eu}^{2+}$  configuration, which is recognized in its magnetic behavior. Such a strong electronic overlap provides the condition for Eu-Eu dimers formation between alternated Eu-NN with the consequent effects on the effective magnetic moments and exchange

interactions. To our knowledge, this unique property was not found till now in any other Eu compound.

We firstly analyze the consequences of such peculiar Eu network on the magnetic and thermal properties in the paramagnetic phase, following with those of the ordered phase whose tentative magnetic phase diagram is proposed. In the former phase the magnetic thermal evidences for Eu-Eu dimers formation are highlighted, and an heuristic function proposed for describing the deviation of the magnetic susceptibility from the standard Curie-Weiss (CW) law below 70 K. The validity of that empirical function is supported by its application on magnetization and specific heat measurements.

The possible formation of a skyrmion lattice, arising from the presence of magnetically frustrated pockets, is analyzed in the proposed magnetic phase diagram according to the alternative phase diagrams proposed by theoretical studies on hexagonal structures, which present similar interactions pattern.

## II. EXPERIMENTAL RESULTS

### A. Paramagnetic phase

#### 1. Low field magnetic susceptibility at intermediate temperature

Although the previous characterization of  $\text{Eu}_2\text{Pd}_2\text{Sn}$  [9] reveals an antiferromagnetic (AF) transition at moderate temperature  $T_N = 13.3\text{ K}$  owing the large effective moment of  $\text{Eu}^{2+}$  atoms:  $\mu_{\text{eff}} = 7.93\mu_B$ , at higher temperatures significant magnetic correlations are triggered. In fact, pure paramagnetic CW behavior of the magnetic susceptibility  $\chi = C_c/(T - \theta)$ , is observed only above cca. 70 K. From that temperature interval a Curie constant  $C_c(T \geq 70\text{ K}) = 7.8\text{ emu K/Eu at. Oe}$  was extracted together with a positive (i.e., ferromagnetic like) paramagnetic temperature  $\theta_p = 18\text{ K}$  [9], see the inset in Fig. 2(b). Despite this, the cusp at  $T = T_N = 13.3\text{ K}$  is the sign of an antiferromagnetic-type transition coexisting with FM interactions revealed by the  $\theta_p > 0$  positive value.

A detailed analysis of the inverse susceptibility ( $1/\chi$ ) reveals a slight positive curvature below about 60 K, see Ref. [9] and Fig. 2(b). Although such a deviation from linear dependence is frequently observed in systems exhibiting magnetic phenomena like spin glass or Kondo effect, they are not expected to occur in this  $\text{Eu}^{2+}$  compound. The periodic lattice distribution of magnetic atoms and on the other hand the stable magnetic moment (with orbital moment  $L = 0$ ) prevent both scenarios.

Since the previous measurements were performed in a magnetic field  $B = 1\text{ T}$ , in order to better investigate the origin of such deviation from the CW behavior further measurements at low field ( $B = 5\text{ mT}$ ) were carried out. The results presented in Figs. 2(a) and 2(b) in the range  $T \leq 70\text{ K}$  reveal more details about that behavior. With that aim we have fitted the experimental data using a modified CW-law function. The two constraints for that heuristic function are: (i) to properly fit the deviation from the observed CW law and (ii) to reproduce it above 70 K. Since the system is expected to continuously change from its high-temperature HT ( $T \geq 70\text{ K}$ ) paramagnetic configuration to another (at  $T = T_N$ ), the most general formula contains the two main temperature-dependent

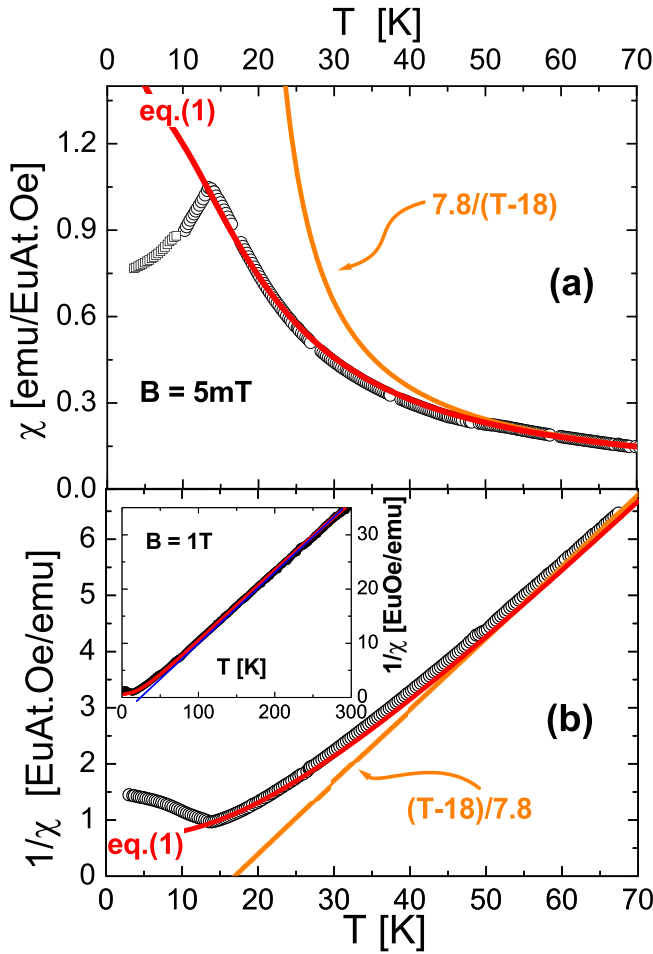


FIG. 2. (a) Deviation of  $\chi(T)$  from the high-temperature CW law (orange curve) described by a modified CW law [Eq. (1), red curve]. (b) Corresponding inverse susceptibility representations. Inset: High-temperature inverse susceptibility compared with fitting functions.

parameters:  $C_c(T)$  and  $\theta_P(T)$ ,

$$\chi(T) = C_c(T)/[T - \theta_P(T)] + \chi_P. \quad (1)$$

Taking into account the HT constraints:  $C_c(T > 70K) = C_{HT} = 7.8$  emu K/Eu at. Oe and  $\theta_P(T > 70K) = \theta_{HT} = 18$  K, the best fit was obtained applying the following temperature dependencies:  $C_c(T) = C_{HT}(1.89 - e^{-\delta/T})$  and  $\theta_P(T) = \theta_{HT} - 24(1 - e^{-\delta/T})$ , with  $\delta = 14$  K and a Pauli-like contribution  $\chi_P = 2 \times 10^{-3}$  emu/Eu at. Oe, see the red curves in Figs. 2(a) and 2(b).

From physical point of view the Boltzmann factor  $e^{-\delta/T}$  represents the thermally driven access from the low-temperature (LT) configuration (dominant at  $T \approx 14$  K) up to a high-temperature one described by the standard CW law. It should be noticed that, although the excitation energy between LT and HT configurations ( $\delta = 14$  K) and the transition temperature ( $T_N$ ) are similar, the former corresponds to a Boltzmann-like energy promotion whereas the latter to a phase transition. In other words, it is evident that under cooling the magnetic phase transition occurs once the LT configuration is sufficiently developed.

Concerning the nature of the LT configuration, two features deserve to be highlighted: the  $C_{LT} = C_c(T \rightarrow 0) = 14.7$  emu K/Eu at. Oe nearly doubles the  $C_{HT}$  value, and the other the negative value of  $\theta_{LT} = -6$  K, which indicates a dominant AF character of the involved interactions. The term  $24(1 - e^{-\delta/T})$  simply describes how the low-temperature AF correlations are overtaken by the FM ones as temperature increases.

For more detailed comparison between HT and LT configurations, it is convenient to identify the involved interactions because they compete in the resultant value of  $\theta_P(T)$ . Taking into account the local coordination of Eu atoms within the puckered-elongated hexagonal layers [see Fig. 1(a)] one can see that the three involved intralayer magnetic interactions ( $K_{ex}$ ) can be described using the terminology proposed for a Kitaev-type scenario [11]. According to the scheme remarked in Fig. 1(a) (the magenta circle),  $K_x$  and  $K_y$  shall indicate the exchange interaction between Eu-NN, which belong to the Eu zig-zag chains, while  $K_z$  refers to the one along the elongate side of the hexagon, i.e., between chains.

The fact that  $\theta_{HT} > 0$  indicates the presence of dominant FM interactions between Eu-NN:  $K_x$  and  $K_y$ . The  $K_z$  interaction is expected not to be so relevant at HT because it acts between chains. As mentioned before, when  $\theta_P(T)$  lowers with decreasing temperature it reveals that such FM interaction is compensated and overcome by an increasing AF interaction. Therefore, as a first approach for competing interactions the observed  $\theta_P$  value corresponds to the additive criterion,  $\theta_P \propto \sum_i K_i$  [13]. It is worth mentioning that the thermal promotion factor  $e^{-\delta/T}$  applied in Eq. (1) was motivated in the Bleaney-Bowers equation [14] for the  $\chi(T)$  dependence of a spin-dimer system composed by two nuclear  $1/2$  spins. In that case the energy gap of the resulting split singlet-triplet levels scheme is temperature independent. This is a strict restriction, because in the process to form a dimer there are two nuclear GS (e.g., two  $s = 1/2$  doublets), which progressively transform into a singlet-triplet system without undergoing a first-order transition. It means that the involved levels change their relative energies during the cooling process driven by an arising magnetic interaction. Consequently, in a real system the energy gap  $\delta$  develops from zero till to stabilize once the dimer is formed. This is the reason to include the  $e^{-\delta/T}$  factor in both temperature-dependent parameters,  $\theta_P(T)$  and  $C_c(T)$ . In this Eu-based compound the mentioned process is certainly more complex than in the Bleaney-Bowers model because the starting GS is highly degenerated,  $N = 2J + 1 = 8$ , due to the large  $J = 7/2$  value involved.

As noticed before, applying Eq. (1) one extracts  $C_{LT} = 1.89 \times C_{HT}$ . This is a relevant result because, according to the possibility of Eu dimers formation, one may analyze it in terms of the Curie constant of a dimer quasiparticle,  $C_D = C_{LT}$ . In that scenario the unit of mass becomes the dimer, i.e., 2 Eu at. Consequently, the dimer's unit of mass is "1 mol" according to the formula unit  $\text{Eu}_2\text{Pd}_2\text{Sn}$ . Therefore, from  $C_{LT} = 1.89 \times 7.8$  emu K/Eu at. Oe the  $C_D = 28.48$  emu K/mol Oe value was obtained.

The total angular momentum of each Eu dimer  $J_D$  depends on the possible projections of the originating orbital moments  $J_{Eu} = 7/2$ . Starting from the maximum possible projection  $J_D = 7$  one can evaluate the ratio between respective Curie

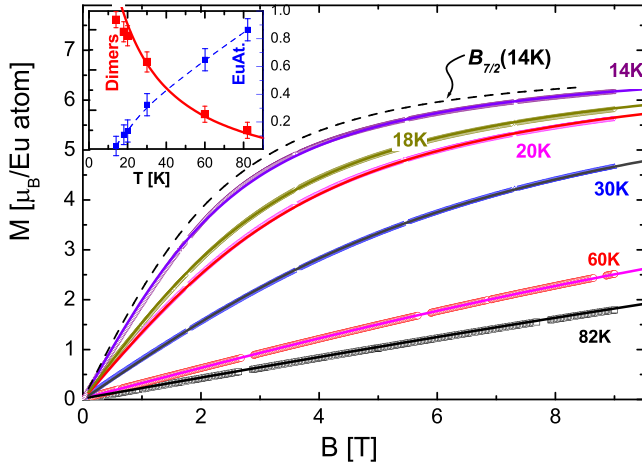


FIG. 3. Magnetization isotherms within the paramagnetic phase ( $14 \leq T \leq 82$  K). Continuous curves on each isotherm represents the fit performed after having weighed  $B_{7/2}$  and  $B_7$  components (see the text). Black-dashed curve compares a pure Brillouin function computed with  $J = 7/2$  at 14 K,  $B_{7/2}(14K)$ , with the experimental results (violet) obtained at  $T = 14$  K. Inset; Red (blue) points, fraction of dimers (single Eu at.) at different temperatures computed from  $M(B)$  data; and continuous red curve, comparison with the function extracted from susceptibility fits using Eq. (1), see the text.

constants  $C_c \propto g_J^2 J(J+1)$  as

$$C_D/C_{HT} = [J_D(J_D + 1)]/[J_{Eu}(J_{Eu} + 1)] \quad (2)$$

where the  $g$  factor is considered constant (i.e., the quantum angular moment remains  $L = 0$ ). With  $J_D$  the ratio between both parameters is  $C_D/C_{HT} = (7 \times 8)/(3.5 \times 4.5) = 56/15.75 = 3.55$ . This ratio is quite close to the experimental one  $28.34/7.8 = 3.78$ . Remember that in this system the mass units are 1 mol = 2 Eu at. for  $C_D$  while it is 1 Eu at. for  $C_{HT}$ . One can confirm that this “maximum” projection,  $J_D = 7$ , is the proper one because the value  $J'_D = 6$  would give a quite smaller ratio of 2.66.

In the scenario of Eu dimers quasiparticles, one has to consider that  $K_x$  and  $K_y$  interactions change their meaning because high-temperature Eu chains transform into the dimer chains. Consequently, approaching  $T_N$  one may identify  $K_x$  as the FM-intradimer interaction and  $K_y$  as the AF-interdimer one. Therefore, from the observed  $\theta_P(T < 70$  K) evolution one learns that the AF- $K_y$  interaction becomes dominant because the FM- $K_x$  (in the paramagnetic phase) becomes part of the dimer structure. At this point it is evident that the physics of dimers formation is complex enough to require a full theoretic development, particularly for  $J > 1/2$  cases.

## 2. Isothermal magnetization above $T_N$

Similar phenomenon emerges in magnetization vs field studies within the same range of temperature. In Fig. 3, isothermal magnetization curves measured between  $\approx T_N$  (i.e., 14 K) and 82 K are shown. The experimental curves can be quite well fitted at 82 K with the paramagnetic Brillouin function,

$$B_J(x) = (a/b) / \tanh[(a/b)x] - (1/b) / \tanh[x/b] \quad (3)$$

where  $a = (2J + 1)$ ,  $b = 2J$ , and  $x = gJ_{Eu}\mu_B B/k_B T = 4.66 \times (B/T)$  applying the  $g_J = 2$  and  $J_{Eu} = 7/2$  values.

However, using this  $J_{Eu}$  factor in Eq. (3), the calculated curve for lower-temperature isotherms progressively deviates from the measured magnetization. In Fig. 3 the  $M(B)$  results at  $T = 14$  K (violet points) are compared with the computed (dashed) curve labeled  $B_{7/2}(14K)$ . Alternatively, a better fit of  $M(B)$  at that temperature is obtained applying the same function but with a  $J_D = 7$ , i.e.,  $B_7(y)$  and therefore  $y = gJ_D\mu_B B/k_B T = 11.6(B/T)$ , which corresponds to the presence of Eu dimers.

This difference allows to evaluate the dimer's fraction variation as a function of temperature. At intermediate temperature  $82 \geq T \geq 14$  K, both functions  $B_{7/2}(x)$  and  $B_7(y)$  are applied to fit the measured magnetization as follows:  $M = M_{Sat}[E \times B_{7/2}(x) + D \times B_7(y)]$ , where the weight factors represent respective contributions of single Eu atoms ( $E$ ) and Eu-Eu dimers ( $D$ ) with the condition  $E + D = 1$ , and the saturation magnetization  $M_{Sat}(2K, 9T) = 6.85\mu_B$  [9].

In order to check the validity of the heuristic function proposed in Eq. (1), in the inset of Fig. 3 we have compared the variation of the fraction of dimers increase by cooling (red curve), using that formula with the values (red points) extracted from the  $M(B, T)$  fits performed applying Eq. (3). This comparison is based on the fact that  $C_C(T) \propto \mu_{eff}^2$  and therefore the number of dimers can be evaluated as  $[C_{HT}(1.89 - e^{-14/T}) - C_{HT}]^{1/2}$ . The comparison between those temperature dependencies is the main feature that supports the proposed heuristic function.

According to  $M(B)$  results, dimer's condensation starts above 80 K and concludes at  $T_N = 13.3$  K, see inset in Fig. 3 where the red curve represents this evolution according to Eq. (1). This process begins at a temperature above which the extrapolated  $\theta_P = 18$  K reveals the presence of a dominant FM exchange interactions  $K_{x,y} > 0$  between Eu-NN and ends at  $T_N$  where  $K_x \neq K_y$ . There, the FM- $K_x$  interactions provides the condensation of Eu dimers and it is progressively overcome by an increasing AF-interdimer interaction  $K_D$  that causes the observed thermal dependence of  $\theta_P(T)$ .

## 3. Specific heat and entropy

The specific heat  $C_P(T)$  dependence of  $\text{Eu}_2\text{Pd}_2\text{Sn}$  was measured in the temperature range of 2–300 K. Above around 60 K the lattice contribution ( $C_{Latt}$ ) is notably well fitted accounting only for phonon ( $C_{Deb}$ ) and band electrons ( $\gamma_{bd} * T$ ) components,  $C_{Latt} = C_{Deb} + \gamma_{bd} * T$ . Respective contributions are described by a Debye function with a Debye temperature  $\theta_{Deb} = 177$  K and  $\gamma_{bd} = 25$  mJ/molK<sup>2</sup> typical for band electrons, see the Fig. 4(a).

At lower temperatures ( $T < 60$  K) the localized  $4f$  electrons of Eu atoms start to contribute,  $C_{LT} = C_P - C_{Latt}$ . However, the corresponding entropy evaluation up to about 60 K,  $S = \int_{0K}^{60K} C_{LT}/T dT$ , exceeds the expected value for  $(2J + 1)$  degeneracy of  $\text{Eu}^{2+}$  GS,  $2R \ln(8)$ , by about 10%, see blue points in Fig. 4(b), where  $R$  is the gas constant. Such an excess of entropy can be calculated by an Einstein-type contribution ( $C_E$ ) [15] as the difference between  $C_{LT}$  and  $C_{4f}$



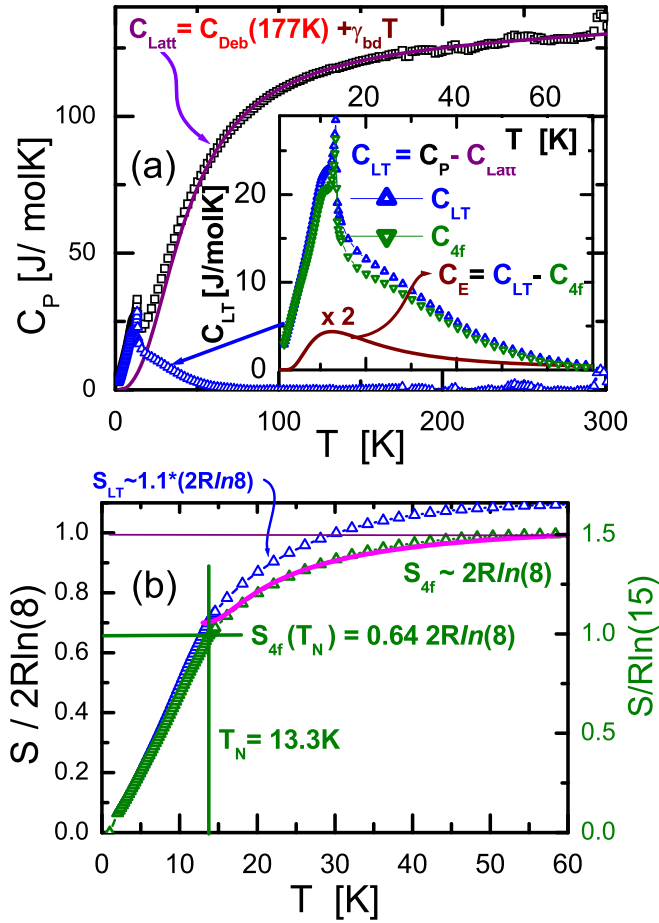


FIG. 4. (a) Measured specific heat up to room temperature described by a Debye function (with  $\theta_{\text{Deb}} = 177$  K) and an electronic band  $\gamma_{\text{bd}} * T$  contribution (see the text). Inset: Low-temperature specific heat contribution ( $C_{\text{LT}}$ , blue points) after phonon and electron band subtraction, and an Einstein-type soft phonon contribution  $C_E$  (multiplied by 2 for clarity, brown curve). (b) Entropy evolution before ( $S_{\text{LT}}$ , blue points) and after ( $S_{4f}$ , green points) the soft phonon contribution subtraction. Continuous (magenta) curve between  $T_N$  and 60 K represents the increase of single Eu at. particles according to the temperature variation proposed for Eq. (1) after the corresponding normalization, see the text.

with an excitation energy  $\Delta = 30$  K, see the inset of Fig. 4(a),

$$C_E = R(2/5)\omega(\Delta/T)^2 e^{\Delta/T} / [1 + \omega * e^{\Delta/T}]^2. \quad (4)$$

The specific heat dependence does not provide direct microscopic information concerning the origin of such proposed soft phonon. Nevertheless, the (2/5) prefactor indicates that this excitation only involves two of the five atoms of the formula unit, e.g., the two Eu or two Pd atoms. A complementary information is provided by the fact that the factor  $\omega = 1/2$  indicates a double degeneracy of the excited level [16,17]. This energy levels degeneracy distribution agrees with dimers formation because at low temperature there is only one possible configuration (one quasiparticle) whereas the excited state corresponds to two particles.

Thus, to obtain the contribution of pure 4f electrons  $C_{4f}$ , the soft phonon contribution  $C_E$  was subtracted as  $C_{4f} = C_{\text{LT}} - C_E$ . The  $C_{4f}$  plot is presented with the green points in

the inset of Fig. 4(a). Now the associated entropy is the expected value  $S_{4f} = 2 R \ln 8$  as shown in Fig. 4(b). Notably, the entropy value at  $T = T_N = 13.3$  K:  $S_{4f}(T_N) = 0.64 \times 2 R \ln 8$  equals  $R \ln 15$ , which corresponds to the entropy of a dimer with total angular momentum  $J_D = 7$ . Consequently, the remnant entropy gain between  $T_N$  and  $T \approx 50$  K ( $2 R \ln 8 - R \ln 15$ ) is the entropy condensed along the Eu dimers formation process.

The coherence between specific heat and magnetic properties can be checked in similar way than with the magnetization, i.e., following the variation the number of degrees of freedom (entropy) above  $T_N$ . As the dimers transform into two single Eu atoms, the entropy increases from  $S(T_N) = R \ln(15)$  to  $S_{\text{HT}} = 2 R \ln(8)$ . Normalizing the entropy at  $T_N$  and at high temperature, and applying the proposed Boltzmann-like thermal variation, one can describe  $\Delta S_{4f}(T) = S(T_N) + 0.36 \times e^{[-\delta/(\eta(T-T_N))]}$  as the magenta curve included in Fig. 4(b) for  $S_{4f}$ . Interestingly, it was needed to include a factor  $\eta = 1.4$  multiplying  $T$  to obtain a good fit. This indicates that a standard Boltzmann factor does not describes properly the ratio of dimers formation as a function of temperature that occurs somehow faster. Nevertheless, to search for an exact function for this process exceeds the aim of this paper, which is to check the formation of dimer particles using an empirical approximation.

Specific heat results provide relevant information upon the phase transition through the jump  $\Delta C_{4f}(T_N) = 28$  J/mol K depicted in the inset of Fig. 4(a). From the mean-field theory [18] for the case of  $J_{\text{Eu}} = 7/2$  the  $\Delta C_{4f}(T_N) = 20.1$ /Eu at. K and it is only slightly increased for  $J_D = 7$ . However, because nearly 1/3 of the degrees of freedom are already condensed at  $T_N$  [ $S_{4f}(T_N) = 0.64 \times 2 R \ln 8$ ], the expected  $\Delta C_{4f}(T_N)$  jump is  $\approx 13$  J/Eu at. K  $\approx 26$  J/mol K, very close to the value observed experimentally.

The formation of Eu-dimer quasiparticles is therefore the most relevant message obtained from the analysis of the magnetic and thermal properties of the paramagnetic phase of this compound. This finding is in agreement with the exceptionally strong Eu-Eu electronic overlap mentioned in Sec. I after considering the reduced Eu-NN spacing within the chains.

## B. Magnetically ordered phase

### 1. Magnetic susceptibility

The magnetic susceptibility  $\chi(T)$  was measured in detail below 25 K, increasing the magnetic field in steps of  $\Delta B = 0.2$  T. In Figs. 5(a) and 5(b), those measurements are represented in steps of 0.2 T up to 1.6 T for clarity, and as labeled up to  $B = 6$  T. At the lowest fields  $B = 0.05$  T, a clear maximum at  $T = T_N = 13.3$  K is observed, which is followed by a weak shoulder at 10 K as the field increases up to  $B = 1.6$  T, see Fig. 5(a).

In order to make more evident the effect of the magnetic field on this system, the temperature derivative  $\partial \chi / \partial T$  was computed in the range  $0 \leq B \leq 2.2$  T, and depicted in Fig. 5(c). There, one can see how the  $\partial \chi(T_N) / \partial T$  peak decreases in intensity whereas a dome starts to increase for  $B \geq 0.6$  T around 10 K and progressively shifts towards lower temperature.

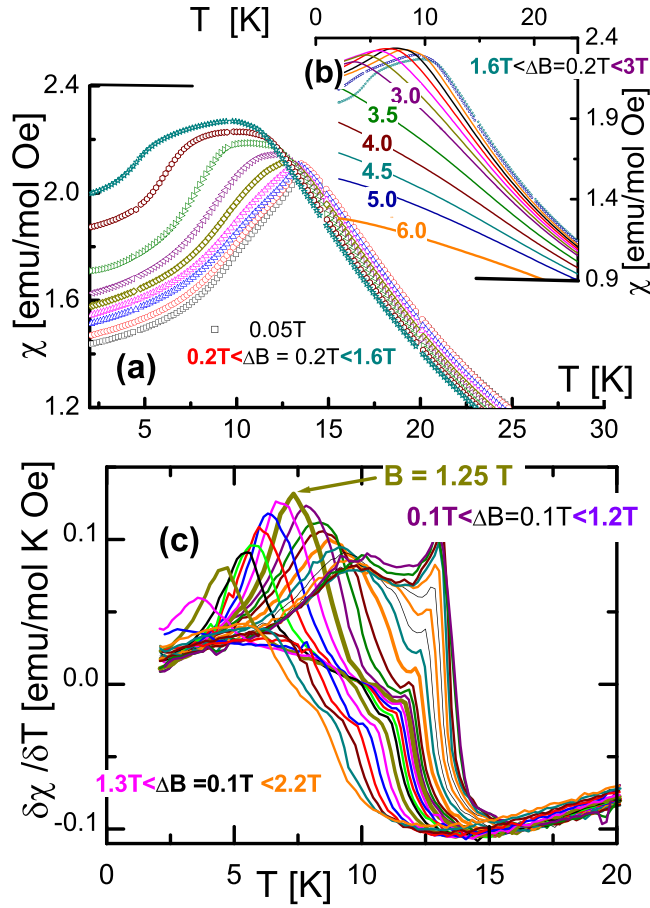


FIG. 5. Detailed isodynas at constant field of magnetic susceptibility as a function of temperature. (a) With the lowest field  $B = 0.05$  T and every  $0.2$  T between  $B = 0.2$  and  $1.6$  T showing the development of a shoulder below  $T_N$ . (b) Every  $\Delta B = 0.2$  T between  $B = 1.6$  and  $3$  T, and as labeled up to  $B = 6$  T. (c) Temperature derivative curves with  $\Delta B = 0.1$  T up to  $20$  K in the range  $0.1 < B < 2.2$  T. The curve for  $B = 1.25$  T is added to highlight the critical field.

Moreover, above  $B \approx 1$  T the susceptibility reveals further modifications. Increasing the field, the  $\partial\chi/\partial T$  dome sharpens showing a maximum intensity at  $B_{cr} = 1.25$  T and  $T_{cr} = 7.3$  K, see Fig. 5(c). Above that critical field the  $\partial\chi/\partial T$  dome decreases in temperature and intensity till to vanish around  $B = 2$  T.

## 2. Magnetization

According to the results presented in Ref. [9] in the ordered phase  $M(B)$  increases quite, but not strictly, linearly between  $0 \leq B \leq 2.5$  T, see Fig. 6(a) (left axis). Once above  $B \approx 3$  T,  $M(B)$  tends to saturate at  $M_{sat}(2\text{ K}) = 6.85\mu_B/\text{Eu at.}$  value.

Due to the polycrystalline character of the samples eventual anisotropic effects can be highlighted analyzing the  $\partial M/\partial B$  derivative. In the case of linear  $M(B)$  contribution in one (or two) directions their respective derivatives shall be field independent and therefore this procedure allows to reveal details of field dependence on the anisotropic one. In this case, the changes in the  $M(B)$  slopes are well identified as it is shown in Fig. 6(a) (right axis) for the  $T = 2$  K curve.

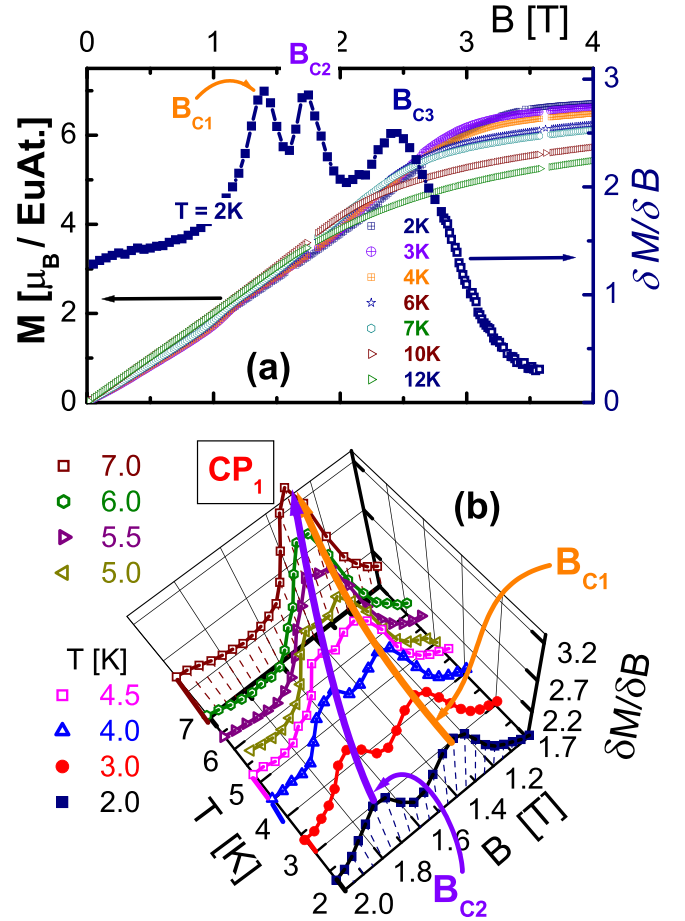


FIG. 6. (a) Left axis:  $M(B)$  results within the ordered phase ( $2 \leq T \leq 12$  K) measured up to  $B = 4$  T. Right axis: Example of the  $\partial M/\partial B$  derivative at  $T = 2$  K, indicating the critical fields. at respective maxima. (b) 3D representation of respective  $\partial M/\partial B$  derivatives between  $2 \leq T \leq 7$  K and  $1.1 \leq B \leq 2$  T ranges. Curves labeled as  $B_{c1}$  (orange) and  $B_{c2}$  (violet) follow respective maxima of the  $\partial M/\partial B$  peaks showing their convergence into a critical point  $CP_1$  at  $T_1 = 7$  K and  $B_1 = 1.25$  T.

The two peaks at  $B_{C1}$  and  $B_{C2}$ , and the maximum at  $B_{C3}$  sign the changes the  $M(B)$  slope, indicating the presence of critic field and the anisotropy in at least one of the axes.

In Fig. 6(b) the  $\partial M/\partial B$  isotherms are presented in a three axes (3D) representation within the  $2 \leq T \leq 7$  K and  $1.1 \leq B \leq 2$  T ranges. There, one can appreciate the evolution of two characteristic maxima related to respective critical fields:  $B_{C1}$  running from  $B = 1.4$  T at  $2$  K to  $B = 1.25$  T at  $7$  K, and  $B_{C2}$  going from  $B = 1.8$  T at  $2$  K to  $B = 1.25$  T at  $7$  K. Both curves merge at a critical point ( $CP_1$ ) at  $B_{cr1} = 1.25$  T and  $T_{cr1} = 7$  K. With further increase of the temperature, a single curve follows up to  $B = 0.9$  T at  $11$  K (not shown for clarity). The third critical curve  $B_{C3}$  passes from  $B = 2.45$  T at  $T = 2$  K, Fig. 6(a), to  $B = 1.15$  T at  $T = 12$  K [not included within the range of Fig. 6(b)].

## 3. Magnetoresistance

The magnetoresistance (MR) presented in Fig. 7 clearly exhibits two different regimes, above and below  $T_N$ . In the paramagnetic region (i.e.,  $T \geq T_N$ ) a broad minimum centered

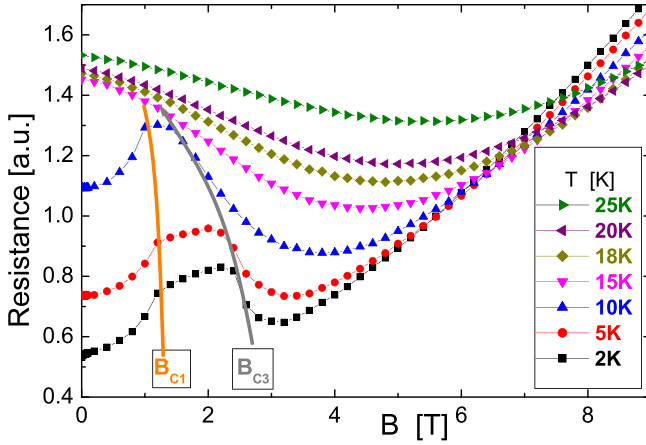


FIG. 7. Magnetoresistance at different temperatures up to  $B = 9$  T, showing how critical fields  $B_{C1}$  and  $B_{C3}$  converge between  $T = 10$  and  $15$  K around  $B = 1.2$  T.

around  $B = 5$  T indicates the scattering with short-range interactions that are progressively suppressed by field. These magnetic correlations can be associated to the competition between FM-intradimer and AF-interdimer interactions as  $T \rightarrow T_N$ .

Such a behavior is strongly modified within the magnetically ordered phase, where a well-defined plateau starts to develop at around  $T_N$  and  $B \approx 1$  T, which expands by decreasing temperature down to  $T = 2$  K. The borders of this plateau can be associated to the two mentioned critical fields,  $B_{C1}$  and  $B_{C3}$ , which converge in the already identified critical point CP<sub>2</sub> at  $T_{cr2} = 12$  K and  $B_{cr2} = 1.15$  T. In these series of measurements the critical field  $B_{C2}$  cannot be distinguished from  $B_{C1}$ .

#### 4. Specific heat

Within the ordered phases, the specific heat of magnetic elements with large  $J > 3/2$  values show a shoulder at about  $1/3$  of  $T_N$ , which is originated in the increasing Zeeman splitting of the manifold GS levels of the paramagnetic state driven by the arising internal molecular field. This effect is particularly observed when there is not CEF effect present [19] and therefore the most prominent examples for this scenario are  $\text{Gd}^{3+}$  and  $\text{Eu}^{2+}$  based compounds with  $J = 7/2$ , see for example Refs. [6,20,21].

In the case of  $\text{Eu}_2\text{Pd}_2\text{Sn}$  such shoulder is quite weak as it can be recognized in Fig. 8(a) in comparison with that of the mean field (MF) prediction (blue curve). In this case it can be seen around 4.5 K in a  $C_{4f}/T$  representation, see Fig. 8(b). At a first glance the  $C_{4f}(T)$  dependence looks quite linear below about 7.5 K suggesting a continuous spectrum of excitations instead of the Zeeman-like distribution of levels. For a more detailed analysis, we have fitted the low-temperature ( $T < 5$  K) range with the function:  $C_{\text{fit}} = \alpha T e^{-g/T} + \beta T^2$ , see green curve in Fig. 7(a). The large coefficient  $\alpha = 1.5$  J/mol K<sup>2</sup> reveals a high density of excitations, only limited at low energy by a small gap of anisotropy  $g = 0.3$  K. The term  $\beta T^2$ , with  $\beta = 0.09$  J/mol K<sup>2</sup>, is a correction to account for the onset of the slight hump around 4.5 K.

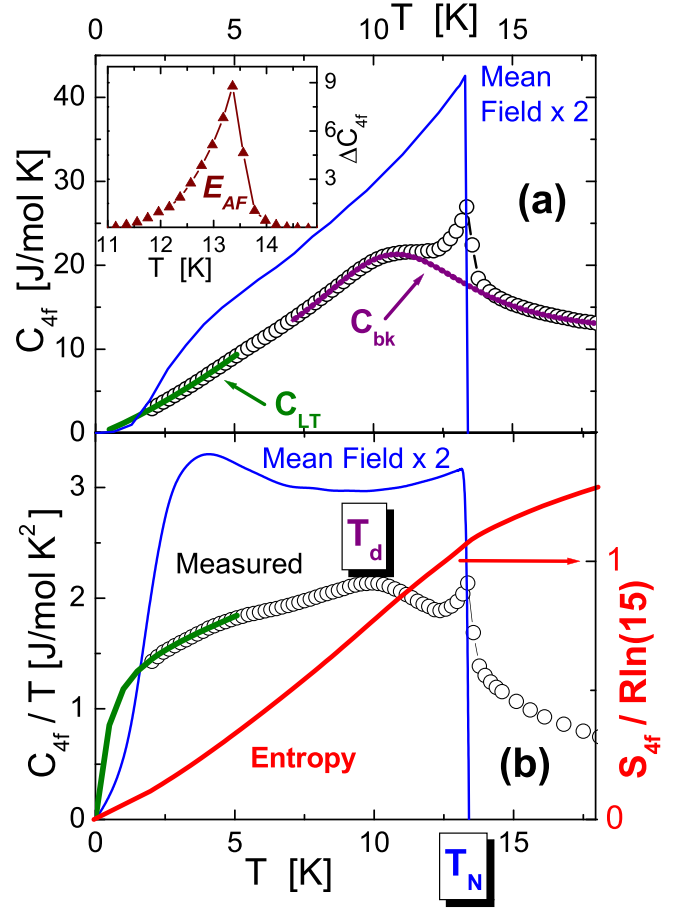


FIG. 8. (a) Detail of the  $4f$  contribution to specific heat in the ordered phase. Green curve ( $C_{LT}$ ): low-temperature fit highlighting quasilinear temperature dependence with small gap at  $T \rightarrow 0$ . Purple curve:  $7 \leq T \leq 20$  K background ( $C_{bk}$ ) fit to evaluate the enthalpy  $E_{AF}$  involved in the transition, see the text. Blue curve: mean field prediction for a  $J = 7/2$  system [19]. Notice that the factor “x2” is included because of the mol = 2 Eu at. units. Inset:  $\Delta C_{4f}$  curve after  $C_{bk}$  subtraction, see the text. (b) Left axis: Measured specific heat divided temperature compared with mean field prediction (blue curve) for  $J = 7/2$ . Green curve:  $C_{LT}/T$  representation of the low-temperature fit. Right axis: (red curve) temperature dependence of the entropy normalized to  $R \ln(15)$ .

These parameters are compatible with a low dimensional AF order [17], including helical order [22].

On the other hand, measured  $C_{4f}(T)$  exhibits a well-defined dome at  $T_d = 10$  K, which is not predicted by the MF description but for modulated magnetic structures, which depend on the relative magnitude of the involved exchange couplings [13].

Concerning the magnetic field dependence, the  $4f$  electronic contribution to specific heat  $C_{4f}(T, B)$  was previously reported in Ref. [9]. Those results are collected in a 3D representation of  $C_{4f}/T$  in Fig. 9(a), where the AF transition  $T_N(B)$  and the temperature of the dome  $T_d(B)$  are traced as a function of magnetic field.

The sharp peak of  $C_{4f}(T_N)/T$  in the figure is observed up to  $B = 1$  T. Beyond that field it transforms into a shoulder. With the aim to investigate whether the sudden increase of that

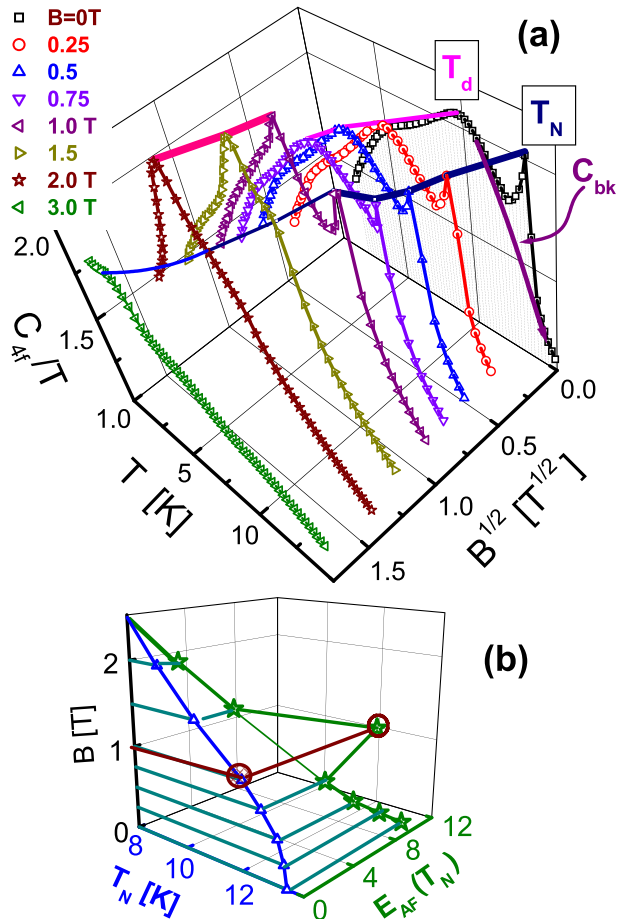


FIG. 9. (a) 3D representation of temperature and field dependence of  $4f$  electrons contribution to specific heat, remarking the AF transition  $T_N(B)$  (blue curve) and the dome  $T_d(B)$  (magenta and pink curves) variations. The purple curve at  $B = 0$  represents the  $C_{bk}(T)$  fit from Fig. 8(a). Notice that the magnetic field axis is defined as the square root  $B^{1/2}$  for a clearer distribution of the curves. (b) 3D representation of the enthalpy  $E_{AF}$  associated to the  $T_N(B)$  transition (see the text) showing the strong increase at  $B = 1$  T (brown lines).

peak at  $T_N$  (12 K, 1 T) has the character of a critical point, we have evaluated the related enthalpy  $E_{AF}(T_N, B)$  by subtracting a background specific heat  $C_{bk}(T, B)$  to the measured  $C_{4f}(T)$ . Such a background is defined by a continuous curve, which fits [23] the measured  $C_{4f}(T)$  above and below  $T_N$  within a range of  $T = T_N \pm 0.1T_N$ , see the purple  $C_{bk}(T)$  curve in Fig. 8(a) and in Fig. 9(a) for the case of the  $C_{4f}(T, 0)$ .

The extracted enthalpy of the transition is computed as  $E_{AF} = \int (C_{4f} - C_{6k}) dT$  and depicted in Fig. 9(b) as a function of magnetic field and  $T_N(B)$ . One can appreciate how  $E_{AF}(T_N, B)$  decreases monotonously from about 8 J/mol at  $B = 0$  to zero at  $B \approx 2.5$  T. However, at  $B = 1$  T a significant increase up to  $E_{AF} = 11.6$  J/mol is observed. It indicates the presence of a singularity likely related to another critical point CP<sub>2</sub> at  $T_N(12$  K, 1 T).

Figure 9(a) shows that the shoulder identified as  $T_d(B < 1T)$  (magenta curve) turns into a sharp peak, which holds up to  $B = 2$  T (pink curve) as a function of  $T$ .

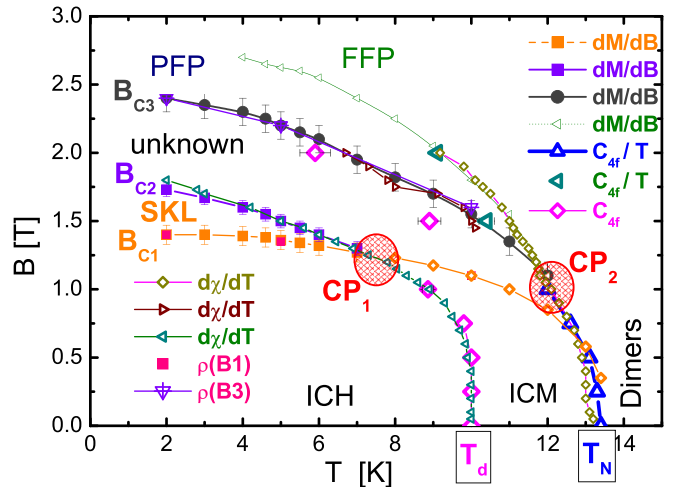


FIG. 10. Magnetic phase diagram of  $\text{Eu}_2\text{Pd}_2\text{Sn}$  where different phase boundaries are defined by respective anomalies in magnetic, thermal, and transport properties. Three main critical fields are included:  $B_{C1}$  and  $B_{C2}$ , that converge in a critical point  $\text{CP}_1$  (7 K, 1.25 T), and  $B_{C3}$  that ends on the critical point  $\text{CP}_2$  (12 K, 1.15 T). Two phase boundaries arise from  $B = 0$ :  $T_d(B)$  indicated by the dome traced in Fig. 8(a) and by the AF transition  $T_N(B)$ . The magnetic structures tentatively proposed for the different phases are: ICM (incommensurate modulated [5]), ICH (incommensurate helicoidal), SKL (skyrmion lattice [28]), PFP (partially field polarized), and FFP (fully field polarized).

### III. DISCUSSION

Starting from the high-temperature configuration one observes that “right” and “left” Eu-Eu interactions within the Eu chains have the same energy since  $K_x = K_y$ . However, once the dimer condenses, there is only one remnant configuration left because one of those interactions (previously identified as  $K_x > 0$ ) has driven the quasiparticle formation. The other ( $K_y$ ) plays the role of the interdimer interaction along the chains. A schematic representation of this  $T \rightarrow T_N$  configuration is depicted in Fig. 11 (see below). This description is in agreement with the temperature dependence of  $\theta_P(T)$ . While its high-temperature ( $T \geq 70$  K) positive value reflects the FM- $K_{x,y} > 0$  of all Eu-NN interactions, the slightly negative value at  $T \rightarrow T_N$  results from the arising interdimer AF- $K_y < 0$  interaction.

Such a strong modification of both  $K_{x,y}$  interactions may trigger the claimed soft phonon as a sort of magnetoelastic effect reflected in a slight displacement of alternated Eu. In fact that the symmetric (“right” and “left”) interatomic bonds along the chain above 70 K is replaced by one *intradimer* bond in one direction of the chain and one *interdimer* interaction in the opposite one.

### A. Magnetic phase diagram

Figure 10 presents the collected experimental information on magnetic, thermal, and transport properties of  $\text{Eu}_2\text{Pd}_2\text{Sn}$  in a magnetic phase diagram. Starting from the low-temperature region, two critical fields,  $B_{C1}$  and  $B_{C2}$ , are well described by respective peaks in  $\partial M/\partial B$  and related maxima in  $\partial \chi/\partial T$  derivatives. Both phase boundaries converge on a critical point



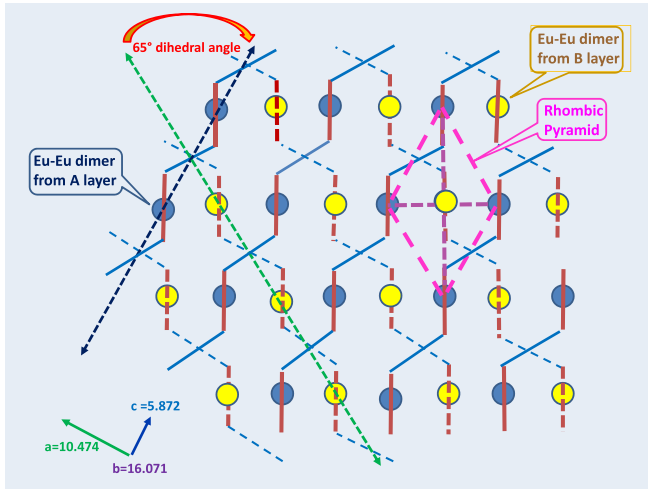


FIG. 11. Reformulation of  $\text{Eu}_2\text{Pd}_2\text{Sn}$  magnetic structure based on dimer's zig-zag chains included in two consecutive layers, represented by blue circles for layer A and yellow ones for layer B. Long dashed arrows (blue and green) indicate the  $65^\circ$  dihedral angle between chains [9]. The rhombic pyramid (magenta-dashed lines) indicate the triangular configuration between dimers belonging to two consecutive layers.

$\text{CP}_1$  at  $T_{cr1} = 7$  K and  $B_{cr1} = 1.25$  T. Other two lines end on that  $\text{CP}_1$ , one related to the  $T_d(T, B)$  dome observed in specific heat and  $\partial\chi/\partial T$ , and the other to a kink in  $\partial\chi/\partial T$ .

The second critical point  $\text{CP}_2$  was identified through the sudden increase of the enthalpy in the  $T_N(B)$  transition presented in Fig. 9(b). A further characteristic field curve, related to an edge in the  $\partial M/\partial B$  slope  $B_{C3}$  runs from  $B = 2.45$  T at  $T = 2$  K and converges on  $\text{CP}_2$  at  $T_{cr2} = 12$  K and  $B_{cr2} = 1.15$  T. At higher fields, a sort of split in  $\partial\chi/\partial T$  indicates the limit of the region where the fully polarized (FM-FP) paramagnetic moments begins and vanishes around 4 K.

### B. Searching for the identity of each magnetic phase

Although the different phase boundaries determined by present thermodynamic and transport results are quite well defined, the polycrystalline nature of the sample blurs any direct information about the anisotropy of their magnetic structures. This handicap can be relieved by analyzing the anisotropic effects in systems with very similar behavior. One of the most appropriate cases is  $\text{EuNiGe}_3$ , studied on single crystals [5,21], which exhibits significant coincidences with our  $\text{Eu}_2\text{Pd}_2\text{Sn}$  like (i) it crystallizes in noncentrosymmetric structure, (ii) it orders AF at the same temperature ( $T_N = 13.2$  K), (iii) that transition is followed by a broad hump at  $T_d = 10.5$  K, and (iv) it shows equivalent jumps in magnetoresistance. These similarities converge into a very similar phase diagram. Notably, the step-like increase of the magnetization clearly observed in  $\text{EuNiGe}_3$  [21] is in full coincidence with that obtained from the  $\partial M/\partial B$  of  $\text{Eu}_2\text{Pd}_2\text{Sn}$ .

A relevant information can be extracted from the 1.8 K isotherm  $M(B)$  of  $\text{EuNiGe}_3$ . The staircase increase on the easy axis of magnetization [001] characterizes a strong anisotropy, whereas on the “ab” plane the  $M(B)$  increases quite linearly up to its saturation value  $M_{sat} = 7\mu_B/\text{Eu at}$ . In polycrystalline

$\text{Eu}_2\text{Pd}_2\text{Sn}$  such a staircase increase is not observed because of the random distribution of the crystals; however, the  $\partial M/\partial B$  derivative [see Fig. 6(a)] transforms the linear  $M(B)$  components into a constants, highlighting the blurred steps as well-defined peaks.

Apart from the mentioned similarities in the jump at  $T_N$  and the dome at  $T_d$ , concerning the specific heat properties there is a remarkable difference in the tail of  $C_{4f}(T)/T$  right above  $T_N$ . Such a difference makes evident that, whereas in  $\text{EuNiGe}_3$  the standard magnetic correlations develop as precursors of the magnetic transition, in  $\text{Eu}_2\text{Pd}_2\text{Sn}$  there is a dimer condensation that largely dominates the scenario above  $T_N$ . In the former compound the typical positive curvature  $C_{4f} \propto T^{-2}$  is observed (see also Refs. [6,13,24,25]), while in the latter there is a nearly linear increase approaching  $T_N$ , see the inset in Fig. 4(a). The consequence of this different condensation of degrees of freedom above  $T_N$  is reflected in respective values of the entropy at  $T_N$ ,  $S_{4f}(T_N) = 0.82 \text{ Rln}(8)$  in  $\text{EuNiGe}_3$  [21], with the remaining entropy reached at 30 K, while in the case of  $\text{Eu}_2\text{Pd}_2\text{Sn}$  it is  $S_{4f}(T_N) = 0.64 \text{ Rln}(8)$ , with the remaining entropy reached at 50 K as indicated in Fig. 4(b). Strictly, this large amount of entropy above  $T_N$  is a “necessary” condition for dimers formation, otherwise there would not be any condensation. This difference is obviously reflected in the  $C_{4f}(T < T_N)$  intensity despite their temperature dependencies look very similar.

Further similarities between these compounds are observed in magnetoresistance (MR) where the most relevant is a sharp plateau in  $\text{MR}(B)$ . Interestingly, this plateau is observed in  $\text{EuNiGe}_3$  with the field applied on the [001] direction only, in agreement with the features detected in  $M(B)$ . Coincidentally, the magnetic phase diagram of  $\text{EuNiGe}_3$  single crystals with field in the  $B//[001]$  direction resembles the one of  $\text{Eu}_2\text{Pd}_2\text{Sn}$  polycrystals, including the critical points identified in Fig. 10. Further, the magnetic phase diagram of  $\text{EuNiGe}_3$  with  $B$  applied in the [100] direction may explain the presence of the uppermost (vanishing) curve between partially and fully field-polarized spin (PFP and FFP) phases.

All these similarities support the possibility to replicate the different magnetic structures determined in  $\text{EuNiGe}_3$  into the  $\text{Eu}_2\text{Pd}_2\text{Sn}$  phase diagram. For example, some spectroscopic studies performed in the former compound, like  $^{151}\text{Eu}$  Mössbauer spectra [21], provide insight for describing possible scenarios. From those results it is concluded that the 13.2 K transition leads to an Incommensurate (ICM) AF intermediate phase, followed by a transition into a commensurate AF configuration near 10.5 K. Later studies [5] indicate that this compound adopts a complex incommensurate helicoidal (ICH) at low temperature, which transforms into an incommensurate sinusoidal modulate up to  $T_N$ .

### C. Magnetic structure reformulation

As discussed in the introduction and shown in Fig. 1 [9,10], the crystalline structure of  $\text{Eu}_2\text{Pd}_2\text{Sn}$  is particularly complex what makes the study of the involved magnetic interactions quite difficult. Furthermore, once established that Eu chains transform into dimer chains, the topology of this compound is modified by the presence of these condensed quasiparticles. With the aim to review the consequences of this panorama,

we reformulate the  $\text{Eu}_2\text{Pd}_2\text{Sn}$  interactions pattern in Fig. 11 with highlighting the dimer chains in the puckered hexagonal network of Eu atoms. Notice that, while dimer chains are depicted along the “c” axis in layer A, the upper ones (belonging to layer B) are rotated in  $65^\circ$ .

With these these considerations and the results from observed magnetic behavior above  $T_N$ , it is evident that the strongest (FM) interaction occurs between Eu-NN:  $K_x > 0$ , within the Eu zig-zag chains along the “c” crystalline direction. Because of the strong Eu-Eu electronic overlap this interaction is responsible for the Eu-Eu dimers formation

The second magnetic interaction:  $K_y < 0$ , becomes relevant at the AF ordering temperature because it connects neighboring Eu dimers along the chain and drives the formation of modulated or helical ordering. Based on dimers zig-zag chains extended along the “c” direction [see Fig. 1(c)] and the mentioned similarities with thermodynamic and magnetic studies on  $\text{EuNiGe}_3$ , an incommensurate helicoidal ordering appears to be congruent with a possible magnetic structure for  $\text{Eu}_2\text{Pd}_2\text{Sn}$  at zero field.

As described in Fig. 1(a), successive layers are stacked along the “b” crystalline direction in an ABA'B'... sequence, with the Eu dimers chains disposed in a dihedral angle of ca.  $65^\circ$  between neighboring AB layers once projected on the “ac” plane (see the dashed dark-blue and green arrows in Fig. 11). In that figure also the B layer projection is included, with Eu dimers represented by blue circles for layer A and yellow for layer B. Notice that neighboring dimers belonging to the same plane form a regular triangular lattice and build up a rhombic pyramid with the first neighbor of the upper plane in its vertex. The pyramid itself displays four triangular faces that, together with the triangular network in plane, provide geometrical conditions for magnetic frustration. The equivalent rhombic pyramid is formed between A' and B' layers, but shifted in the “ac” plane as depicted in Fig. 1-II of Ref. [9].

#### D. Possible formation of a skyrmions phase

It is well known that by the cooling, frustrated systems are compelled to search for alternative ground states with lower degeneracy in order to reduce its entropy. That constraint favors the access to unexpected phases, which are not reached by standard magnets that order at higher temperatures [26]. Among a variety of possible magnetic configurations, skyrmion vortex lattices provide an alternative to build up some type of coherent structure. Skyrmions are described as rather ubiquitous topological magnetic structures observed in several magnetic materials without inversion symmetry [27].

These topologically stable structures appear as triangular crystals of vortex lines parallel to the field direction, which are manifested as small pockets in the magnetic phase diagram of noncentrosymmetric magnets [28].  $\text{Eu}_2\text{Pd}_2\text{Sn}$  fulfils a number of conditions for the formation of those skyrmion structures: magnetic frustration, modulate type of propagation vector along one direction, which differs around  $120^\circ$  (as the complementary angle to the observed ca.  $65^\circ$ ) with the neighboring chain, and it shows one of those eventual pockets between  $B_{C1}$  and  $B_{C2}$  associated to a critical point  $\text{CP}_1$  in its phase diagram (see Fig. 10). In Ref. [28] a series of alternative magnetic phase diagrams is presented, obtained by Monte

Carlo simulations and computed according to selected values of neighboring magnetic couplings, which produce different propagation vectors. Among the proposed phase diagrams, the one with “moderate adjacent interlayer exchange and zero interaction between NNN layers” (Fig. 1 a in Ref. [28]) also presents a tetracritical point among the similarities observed with  $\text{Eu}_2\text{Pd}_2\text{Sn}$ . Such possibility requires to be confirmed by microscopic magnetic studies performed on single crystal samples.

#### E. Tentative description of the magnetic phases structures

The reformulation of the magnetic configuration based on the presence of Eu dimers presented in Fig. 11, the detailed comparison with  $\text{EuNiGe}_3$  single crystals behavior and the possibility of a skyrmion phase formation allow to proceed towards a reliable identification of some of the magnetic phases presented in Fig. 10.

At zero- and low-magnetic fields, the quasi-paramagnetic phase above the Néel temperature is marked by the dimers formation. Below the transition an incommensurate AF-ICM phase appears, which transforms into an helicoidal incommensurate AF-ICH type of order. Around  $B \approx 1$  T two critical points are observed. One,  $\text{CP}_1$  at  $T \approx 7$  K, with characteristics of tetracriticality, marks the upper temperature limit of the proposed skyrmions lattice phase. The other,  $\text{CP}_2$  at  $\approx 12$  K, marks the limit of the  $T_N(T, B)$  transition, which exhibits signs of first order. Between  $B_{C2}$  and  $B_{C3}$  critical fields there is an unidentified (“unknown”) phase due to the lack of enough information about its nature. Above  $B_{C3}$  the magnetic phases, which be more likely identified as partially FM-PP and fully FM-FP polarized ferromagnets. It is evident that microscopic investigation, like neutron diffraction or Mössbauer spectroscopy, applied on single crystal samples are required to confirm these magnetic structures.

#### IV. CONCLUSIONS

The  $\text{Eu}^{2+}$  network in  $\text{Eu}_2\text{Pd}_2\text{Sn}$  can be represented by zig-zag chains located in puckered elongated hexagons. A distinctive feature of this compound is the reduced atomic distance between Eu atoms into the zig-zag chains compared to that evaluated for pure  $\text{Eu}^{2+}$ . As a result, a strong overlap with the NN electronic cloud is expected, due to which the formation of Eu dimer quasiparticles begins to condense at quite high temperature ( $\approx 70$  K).

Such dimer formation, with a very large  $J_D = 7$  quantum number, allow us to understand the deviation of magnetic susceptibility from the high-temperature CW law at high temperature, together with the deviation of  $M(B)$  from the high-temperature  $B_{7/2}$  Brillouin function and the entropy accumulated at the ordering temperature  $T_N$  confirms this behavior. The robustness of this description is supported by the fit of the  $T$  variation of the number of dimers  $[D(T)]$  deduced from the magnetization (see the inset in Fig. 3) and from single Eu atoms deduced from the increase in entropy  $S_{4f}(T)$  [see Fig. 4(b)] applying the relative thermal weight of electronic configurations extracted from Eq. (1).

The presence of these quasiparticles requires a reformulation of the magnetic structure of the compound, with expected

consequences for the role of the magnetic interactions such as the transformation from a FM dominant interaction at high temperature to an AF one around  $T_N$ .

A rich magnetic phase diagram results from the analysis of the temperature derivatives of the magnetic properties and specific heat as a function of field. Two critical points are derived from this study. The lack of microscopic knowledge of the magnetic nature of these phases can be addressed by comparing its behavior with that of a mirror compound  $\text{EuNiGe}_3$  investigated on single crystal samples. From this comparison it appears that Eu dimers form incommensurated AF chains below the AF transition at 13.3 K. The topological properties

of this configuration provide the conditions for geometric frustration between adjacent dimers of one layer and those of the subsequent one in a rhombic pyramidal configuration.

## ACKNOWLEDGMENTS

This research work is part of the Project implementation: University Science Park TECHNICOM for Innovation Applications Supported by Knowledge Technology, ITMS: 313011D232, supported by the Research & Development Operational Programme funded by the ERDF; and also by VEGA1/0705/20, 1/0404/21.

- [1] J. G. Sereni, Rare earth metals melting temperature anomalies, *J. Phys. Chem. Solids* **45**, 1219 (1984).
- [2] J. G. Sereni, Thermomagnetic properties of very heavy fermions suitable for adiabatic demagnetization refrigeration at low temperature; *Philos. Mag.* **100**, 1211 (2020).
- [3] C. Schwickert, F. Winter, and R. Poettgen, The stannides  $\text{EuPd}_2\text{Sn}_2$ ,  $\text{EuPt}_2\text{Sn}_2$ ,  $\text{EuAu}_2\text{Sn}_2$ , and  $\text{Eu}_3\text{Ag}_{5.4}\text{Sn}_{5.6}$ —Structure and magnetic properties, *Z. Naturforsch. B* **69**, 775 (2014).
- [4] O. Bednarchuk and D. Kaczorowski, Strongly anisotropic and complex magnetic behavior in  $\text{EuRhGe}_3$ , *J. Alloys Compd.* **646**, 291 (2015).
- [5] D. H. Ryan, J. m. Cadogan, Rasa Rejali, and C. D. Boyer, Complex incommensurate helicoidal magnetic ordering of  $\text{EuNiGe}_3$ , *J. Phys.: Condens. Matter* **28**, 266001 (2016).
- [6] W. B. Jiang, M. Smidman, W. Xie, J. Y. Liu, J. M. Lee, J. M. Chen, S. C. Ho, H. Ishii, K. D. Tsuei, C. Y. Guo, Y. J. Zhang, H. Lee, and H. Q. Yuan, Antiferromagnetism with divalent Eu in  $\text{EuNi}_5\text{As}_3$ , *Phys. Rev. B* **95**, 024416 (2017).
- [7] D. G. Franco, Y. Prots, C. Geibel, and S. Seiro, Fluctuation-induced first-order transition in Eu-based trillium lattices, *Phys. Rev. B* **96**, 014401 (2017).
- [8] I. Čurlík, M. Giovannini, F. Gastaldo, A. M. Strydom, M. Reiffers, and J. G. Sereni, Crystal structure and physical properties of the two stannides  $\text{EuPdSn}_2$  and  $\text{YbPdSn}_2$ , *J. Phys.: Condens. Matter* **30**, 495802 (2018).
- [9] M. Giovannini, I. Čurlík, R. Freccero, P. Solokha, M. Reiffers, and J. Sereni, Crystal structure and magnetism of noncentrosymmetric  $\text{Eu}_2\text{Pd}_2\text{Sn}$ , *Inorg. Chem.* **60**, 8085 (2021).
- [10] I. Doverbratt, S. Ponou, Y. Zhang, S. Lidin, and G. J. Miller, Linear metal chains in  $\text{Ca}_2\text{M}_2\text{X}$  ( $\text{M} = \text{Pd}, \text{Pt}$ ;  $\text{X} = \text{Al}, \text{Ge}$ ): Origin of the pairwise distortion and its role in the structure stability, *Chem. Mater.* **27**, 304 (2015).
- [11] A. Kitaev, Anyons in an exactly solved model and beyond, *Ann. Phys.* **321**, 2 (2006).
- [12] Edited by W. M. Haynes, *CRC Handbook of Chemistry and Physics*, 94 ed. (CRC Press, Boca Raton, FL, 2013–2014), Sec. 4, p. 115.
- [13] J. A. Blanco, D. Ginioux, and D. Schmitt, Specific heat in some gadolinium compounds, *Phys. Rev. B* **43**, 13145 (1991).
- [14] B. Bleaney and K. D. Bowers, Anomalous paramagnetism of copper acetate, *Proc. R. Soc. London A* **214**, 451 (1952); S. Blundell, *Magnetism in Condensed Matter* (Oxford University Press, Oxford, 2012), p. 83.
- [15] A. Tari, *The Specific Heat of Matter at low Temperatures* (Imperial College Press, London, 2003).
- [16] The factor  $\omega$  represent the ratio between de ground ( $\omega_0$ ) and excited ( $\omega_1$ ) levels degeneracies:  $\omega = \omega_0/\omega_1$  [17].
- [17] E. S. R. Gopal, *Specific Heats at Low Temperature* (Heywoods Books, London, 1966).
- [18] From mean-field theory, the specific heat jump at  $T_N$  is given by [19]:  $\Delta C(T_N) = 5/2R[(2J+1)^2 - 1]/[(2J+1)^2 + 1]$ . Notice that in the figure the specific heat is presented in [J/mol K] units whereas for this formula  $\Delta C(T_N)$  is expressed in [J/atom K] units.
- [19] P. H. E. Meijer, J. H. Colwell, and B. P. Shah, A note on the morphology of heat capacity curves, *Am. J. Phys.* **41**, 332 (1973).
- [20] N. Kumar, S. K. Dhar, A. Thamizhavel, P. Bonville, and P. Manfrinetti, Magnetic properties of  $\text{EuPtSi}_3$  single crystals, *Phys. Rev. B* **81**, 144414 (2010).
- [21] A. Maurya, P. Boneville, A. Thamizhavel, and S. K. Dahr,  $\text{EuNiGe}_3$ , an anisotropic antiferromagnet, *J. Phys.: Condens. Matter* **26**, 216001 (2014).
- [22] N. S. Sangeetha, E. Cuervo-Reyes, A. Pandey, and D. C. Johnston,  $\text{EuCo}_2\text{P}_2$ : A model molecular field helica Heisenberg antiferromagnet, *Phys. Rev. B* **94**, 014422 (2016).
- [23] The full  $C_{bk}(T)$  curve was obtained by fitting  $C_{4f}$  within the  $5 \leq T \leq 22$  K range using as fitting function:  $C_{bk} = 193/[(T - 10.8)^2 + 14] + 3 * \text{atan}((T - 11.5)/7) + 8$ .
- [24] D. G. Franco and C. Geibel, Synthesis and study of the chiral magnetic system  $\text{EuIr}_2\text{P}_2$ , *Phys. Rev. B* **104**, 054416 (2021).
- [25] R. J. Goetsch, V. K. Anand, and D. C. Johnston, Antiferromagnetism in  $\text{EuNiGe}_3$ , *Phys. Rev. B* **87**, 064406 (2013).
- [26] J. G. Sereni, Entropy constraints in the ground state formation of magnetically frustrated systems, *J. Low Temp. Phys.* **190**, 1 (2018).
- [27] A. Fert, N. Reyren, and V. Cros, Magnetic skyrmions: Advances in physics and potential applications, *Nat. Rev. Mater.* **2**, 17031 (2017).
- [28] S.-Z. Lin and C. Batista, Face Centered Cubic and Hexagonal Close Packed Skyrmion Crystals in Centrosymmetric Magnets, *Phys. Rev. Lett.* **120**, 077202 (2018).